AGU PUBLICATIONS

JGR

Journal of Geophysical Research: Atmospheres

RESEARCH ARTICLE
10.1002/2015JD023266

Key Points:
- Near-kilometer grid spacing best resolves catchment-scale meteorological variability
- Different processes drive seasonal reversal in vertical gradient of precipitation
- Forcing from high-resolution models can potentially improve the local accuracy of impact studies

Correspondence to:
W. W. Immerzeel,
w.w.immerzeel@uu.nl

Citation:
Collier, E., and W. W. Immerzeel (2015), High-resolution modeling of atmospheric dynamics in the Nepalese Himalaya, *J. Geophys. Res. Atmos.*, *120*, doi:10.1002/2015JD023266.

Received 17 FEB 2015
Accepted 12 AUG 2015
Accepted article online 15 AUG 2015

High-resolution modeling of atmospheric dynamics in the Nepalese Himalaya

Emily Collier[1] **and Walter W. Immerzeel**[1]

[1]Department of Physical Geography, Utrecht University, Utrecht, Netherlands

Abstract High-altitude meteorological processes in the Himalaya are influenced by complex interactions between the topography and the monsoon and westerly circulation systems. In this study, we use the Weather Research and Forecasting model configured with high spatial resolution to understand seasonal patterns of near-surface meteorological fields and precipitation processes in the Langtang catchment in the central Himalaya. Using a unique high-altitude observational network, we evaluate a simulation from 17 June 2012 to 16 June 2013 and conclude that, at 1 km horizontal grid spacing, the model captures the main features of observed meteorological variability in the catchment. The finer representation of the complex terrain and explicit simulation of convection at this grid spacing give strong improvements in near-surface air temperature and small improvements in precipitation, in particular in the magnitudes of daytime convective precipitation and at higher elevations. The seasonal differences are noteworthy, including a reversal in the vertical and along-valley distributions of precipitation between the monsoon and winter seasons, with peak values simulated at lower altitudes (~3000 m above sea level (asl)) and in the upper regions (above 5000 m asl) in each season, respectively. We conclude that there is great potential for improving the local accuracy of climate change impact studies in the Himalaya by using high-resolution atmospheric models to generate the forcing for such studies.

1. Introduction

Mountain meteorology is complex, in particular in the Himalayas, owing to intricate interactions between the atmosphere and local topography, synoptic-scale weather systems, and the monsoonal and westerly circulation systems. The central Himalayan region is dominated by a monsoonal climate, in which most of the precipitation falls during summer (June to September) [*Bookhagen and Burbank*, 2010], while winters are rather dry. The interplay between topography and precipitation is complex and manifests itself at various scales ranging from a synoptic scale of several hundreds of kilometers to an orographic mesoscale of less than 30 km [*Barros et al.*, 2004]. From east to west, the monsoon influence decreases and midlatitude westerlies become more important in the western part of the Greater Himalaya (Pamir and Karakoram Ranges). Precipitation from the westerlies is highest in winter, when low-pressure systems reach the western margin of the Greater Himalaya. This supply of moisture reaches higher elevations than the summer monsoon, which might be related to the higher tropospheric extent of the westerly airflow [*Scherler et al.*, 2011].

Accurate information about high-altitude meteorological conditions is essential for understanding regional differences in the Himalaya. In particular, spatially distributed precipitation and air temperature data are key inputs for glacio-hydrological studies. However, observations at high elevations are scarce. Moreover, commonly used gridded precipitation products are grossly inaccurate at these altitudes and are too coarse for high-resolution hydrological assessments [*Palazzi et al.*, 2013]. A common approach for addressing the lack of suitable data is to extrapolate from station data using assumed vertical and horizontal gradients to derive spatial fields of precipitation and air temperature [*Immerzeel et al.*, 2013; *Ragettli et al.*, 2014]. Such rates are commonly calibrated, uncertain, and vary in time and space. Furthermore, while this approach may be appropriate for air temperature under well-mixed free atmospheric conditions, recent work [*Lundquist et al.*, 2008; *Minder et al.*, 2010; *Immerzeel et al.*, 2014] showed that it is inadequate in glacierized catchments in regions of complex topography, since katabatic winds, cold air pooling, and seasonal differences in relative humidity strongly influence the air temperature distribution.

High-resolution atmospheric modeling has the potential to compensate for spatial and temporal gaps in observational networks, to improve the understanding of atmospheric variability in Himalayan catchments,

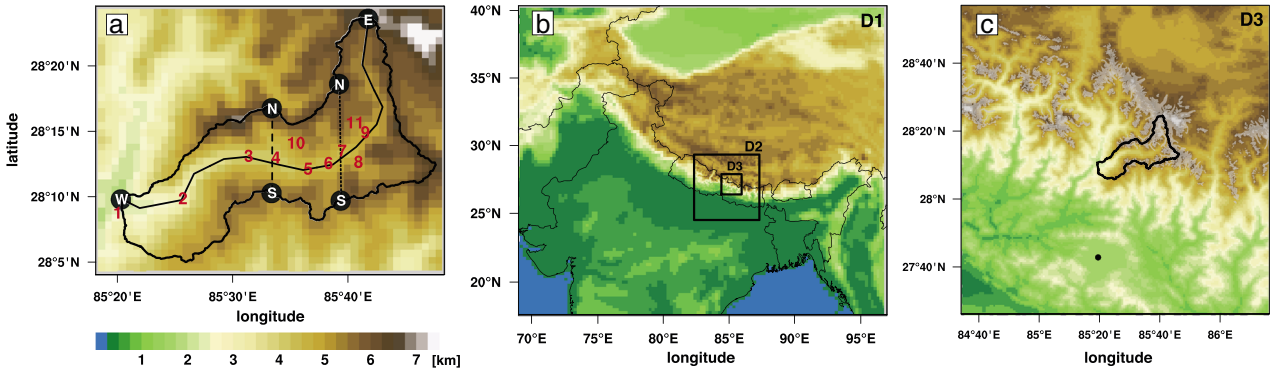

Figure 1. (a) The spatial extent of the Langtang catchment, delineated by the outer black contour. The locations of the 11 observational sites are marked in red. The locations of one along-valley and two cross-valley sections used for computing transects in sections 3.3 and 3.4 are also shown. (b) The spatial extents and modeled topographic height of all three WRF-CMB model domains, which are configured with horizontal grid spacings of 25, 5, and 1 km. (c) A zoom-in of the finest resolution domain, D3, which shows (i) the wider geographic location of the Langtang catchment; (ii) the glacier outlines [*Pfeffer et al.*, 2014], shaded in light grey; and (iii) the location of Kathmandu, indicated by the black circle marker. Figures 1a and 1c show modeled topographic height in D3 (1 km grid spacing) shaded in units of km.

and to provide more accurate distributed temperature and precipitation forcing data for glacio-hydrological studies. Recently, several studies have used the advanced research version of the Weather Research and Forecasting (WRF) model [*Skamarock and Klemp*, 2008] successfully in high mountain Asia. For the High Asia Refined analysis, WRF was applied over the entire Greater Himalayan region at 10 km horizontal grid spacing, and results matched well with precipitation magnitudes and patterns as derived from satellite imagery [*Maussion et al.*, 2014]. The model also reproduced the large-scale interaction between topography and precipitation [*Bookhagen and Burbank*, 2006] and the monsoon and westerly circulation systems. This data set helped to reveal that midlatitude westerlies affect precipitation variability in May and June, which is in turn a key factor in the annual mass balance of glaciers on the Tibetan Plateau [*Mölg et al.*, 2014]. WRF has also been used to (i) study atmosphere-glacier feedback in the Karakoram over an ablation season, revealing that coupling with a process-based glacier model improved the simulation of land surface temperature and snow albedo [*Collier et al.*, 2013], and (ii) analyze precipitation processes during winter extratropical cyclone events [*Norris et al.*, 2015]. These studies join a growing number using mesoscale atmospheric models for glacio-hydrological applications in high mountain Asia [e.g., *Kumar et al.*, 2015] and demonstrate the usefulness of WRF for this region. However, to date studies that integrate high-altitude observations with high-resolution simulations to investigate drivers of catchment-scale meteorological variability in the Himalayas are lacking but highly needed by the glaciological and hydrological communities.

In this study, we use the coupled WRF and glacier climatic mass balance (CMB) model of *Collier et al.* [2013], configured with telescoping nested domains down to 1 km grid spacing, to investigate atmospheric dynamics in a glacierized catchment in Nepal over the period of 17 June 2012 to 16 June 2013. We evaluate the model performance using a high-altitude observational data set and investigate the impact of horizontal resolution on simulated variability in local meteorological conditions. Focusing on the two most contrasting periods, the monsoon and winter seasons, we then assess drivers of precipitation and spatial patterns in the valley, in particular elevational gradients of air temperature and precipitation.

2. Methods

2.1. Study Area and Observational Data

The study area is the Langtang catchment (Figure 1a), which is located in the central Himalaya (Figure 1b). The catchment has an area of 584 km^2, of which 24% is glacier covered. The altitudinal range of the Langtang is 1406 to 7180 m above sea level (asl), with the glacierized altitudes located from 4040 m asl upward. Supraglacial debris is prevalent, with 40% of the glacier area covered. The Langtang River flows through the valley, which is V-shaped in its downstream part and U-shaped in the upper part. Below 3000 m, the catchment is densely forested, while at higher altitudes forest is found at the slopes directly adjacent to the river. Boulders and scree cover are dominant above an altitude of 4000 m asl. We note that debris cover is not accounted for in this study. In addition, the extent of forested areas in the Langtang

Table 1. Observational Site Information

Site	Latitude	Longitude	Elevation (m asl)	Sensor (% Missing)
1	28.1574	85.3322	1406	TB(2.4), TL(18.2)
2	28.1621	85.4307	2370	TB(0), TL(11.4)
3	28.214	85.5275	3539	TB(16.2), TL(10.1)
4	28.211	85.5669	3857	TB(0), TL(57.4)
5	28.1956	85.613	3875	TB(0), TL(15.8)
6	28.2022	85.6428	3981	TB(0), TL(15.8)
7	28.2176	85.6631	4312	TB(92.2)
8	28.2027	85.6862	4452	TB(93.5)
9	28.2401	85.6974	4617	TL(44.2)
10	28.229	85.597	4831	PLU(0), UDG, TS
11	28.253	85.6815	4919	PLU(92.2), UDG, TS

catchment is underestimated by ~60% in the default U.S. Geological Survey (USGS) land use data in WRF compared with the GlobCover data set [*Leroy et al.*, 2007], with these areas instead categorized mainly as cropland, grassland, and shrubland.

A number of field campaigns have been conducted in this region to understand meteorological variability [e.g., *Morinaga et al.*, 1987; *Seko*, 1987; *Ueno and Yamada*, 1990; *Seko and Takahashi*, 1991; *Ueno et al.*, 1993; *Fujita et al.*, 1997]. More recently, a high-altitude observational network of temperature and precipitation was established, which provides data from mid-2012 to present (Figure 1a and Table 1) [*Immerzeel et al.*, 2014]. The network consists of eight tipping buckets, seven temperature loggers, and two pluviometers, which include snow depth and temperature sensors. The details of the sensors, preprocessing, and data quality checks are described in *Immerzeel et al.* [2014]. In the analysis, we made four seasonal divisions based on these data, similar to *Immerzeel et al.* [2014]: the monsoon season from 17 June to 17 September 2012, the postmonsoon season from 18 September to 31 December 2012, the winter season from 1 January to 1 March 2013, and the premonsoon season from 1 March to 16 June 2013. The definition of the monsoon season differs slightly from *Immerzeel et al.* [2014] and is selected based on a marked increase in precipitation in the Langtang and surrounding region, as well as the onset of periods with strong correlation between precipitation and lower level meridional winds.

2.2. Modeling Tool

The simulations were performed using an interactively coupled atmosphere and glacier climatic mass balance model, WRF-CMB [*Collier et al.*, 2013]. The atmospheric component of the coupled model is version 3.6.1 of WRF [*Skamarock and Klemp*, 2008], while the CMB component is based on the model of *Mölg et al.* [2008, 2009]. For this study, the coupled model was configured with three nested domains, with horizontal grid spacings of 25, 5, and 1 km (Figures 1b and 1c). The model has 50 vertical levels between the surface

Table 2. WRF Configuration

Domain Configuration		
Horizontal grid spacing	25, 5, and 1 km (domains 1–3)	
Grid dimensions	125 × 105, 111 × 111, 171 × 171	
Vertical levels	50	
Model top pressure	50 hPa	
Nesting approach	One way	
Model physics		
Radiation	Community Atmosphere Model	*Collins et al.* [2004]
Microphysics	Morrison	*Morrison et al.* [2009]
Cumulus	Kain-Fritsch (none in D2 or D3)	*Kain* [2004]
Planetary boundary layer	MYNN level 2.5	*Nakanishi and Niino* [2006]
Atmospheric surface layer	Monin-Obukhov (revised MM5)	*Jiménez et al.* [2012]
Land surface	Noah-MP	*Niu et al.* [2011]
Dynamics		
Top boundary condition	Rayleigh damping	
Diffusion	Calculated in physical space	
Lateral boundaries		
Forcing	ERA-Interim 0.75° × 0.75°, 6 hourly	*Dee et al.* [2011]

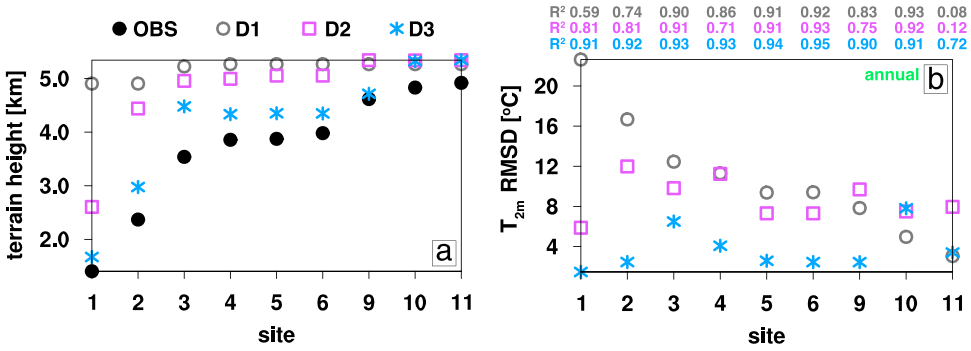

Figure 2. (a) A comparison of real terrain height (black circle markers) with modeled values in D1 (grey circles), D2 (purple squares), and D3 (blue asterisks) for all observations sites with less than 50% of missing data, which are used for point comparisons. The site numbers increase approximately with distance downvalley, with the exception of upslope sites 8, 10, and 11. (b) Annual root-mean-square difference (RMSD) between observed and simulated air temperature (°C) at a height of 2 m. R^2 values are given for each station and model domain as a text string above the panel. For all panels of Figures 2 and 3, data from the stations, D1, D2, and D3 are shown in black, grey, purple, and blue, respectively.

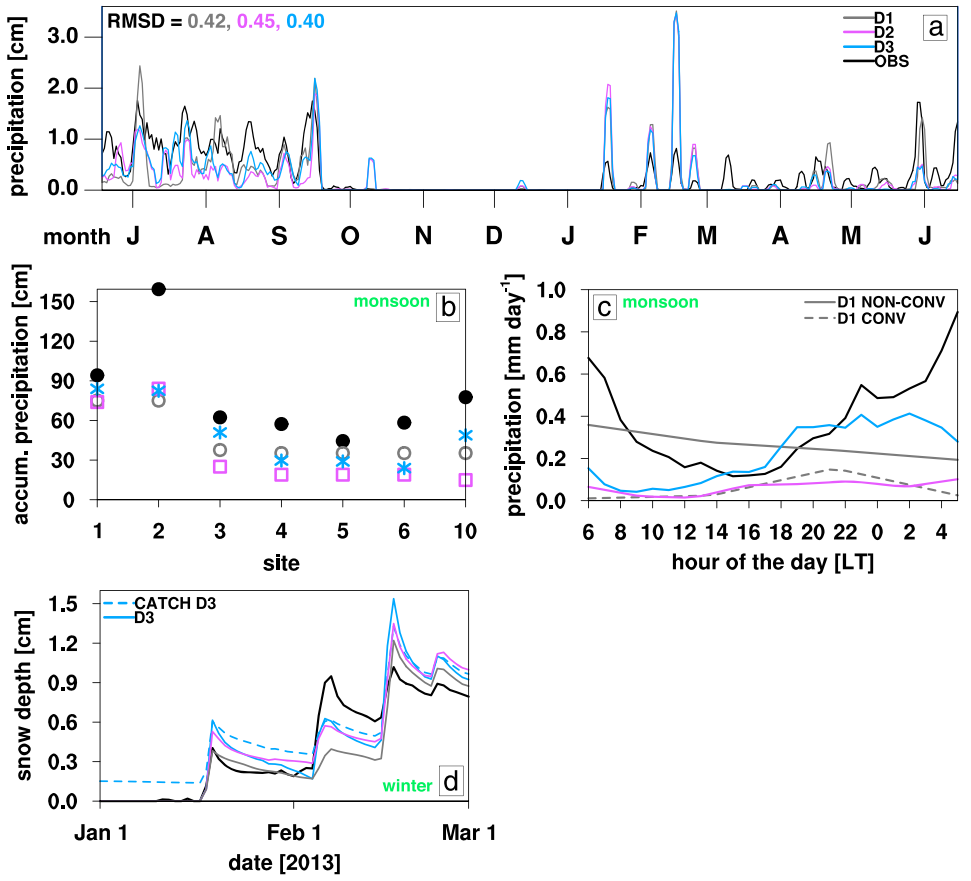

Figure 3. (a) Annual time series of daily total precipitation (cm), averaged over all available observational sites and plotted as a 3 day running average. (b) Accumulated precipitation (cm) over the monsoon period at each observation site. The marker legend for Figure 3b is the same as Figure 2a. (c) The mean diurnal cycle of precipitation during the monsoon period in mm d^{-1} for each model domain, averaged over the sites where observational data are available (sites 1–6 and 10). Note that the diurnal cycle in D1 is divided into its convective (parameterized) and nonconvective (grid scale) components. (d) A time series of snow accumulation during winter at the site with available data, station 10 (black curve), compared with the simulated snow depth at the closest grid point in D1, D2, and D3 (solid curves). Snow depth averaged over the entire catchment in D3 during winter is also shown (dashed curve).

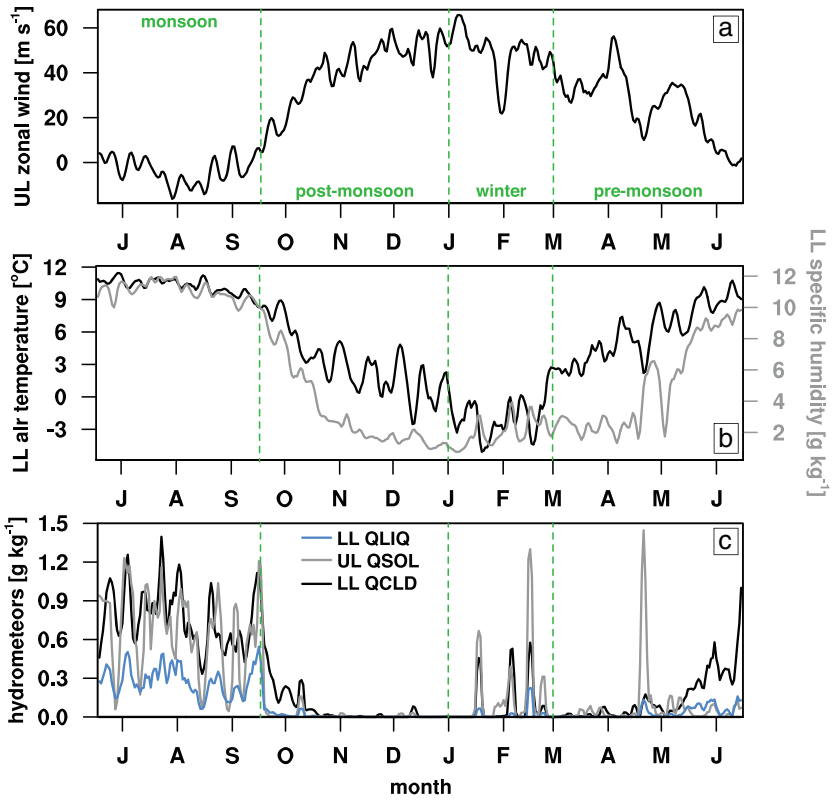

Figure 4. Annual time series of (a) upper level zonal wind (m s^{-1}), averaged from 300 to 150 hPa; (b) lower level air temperature (°C) and specific humidity (g kg^{-1}), averaged over the lowest 100 hPa; and (c) vertically integrated lower level cloud and rainwater mixing ratios (g kg^{-1}), summed over the lowest 100 hPa, and upper level solid hydrometeors (snow, ice, and graupel), summed from 500 to 100 hPa. Data are area averaged over D3 and plotted as 3 day running averages.

and 50 hPa, including 11 located on average in the lowest 1 km above ground, with the first model level specified at ~35 m.

The model physics were selected on the basis of short test simulations in both the summer and winter seasons (1–10 July 2012 and 10–20 January 2013, respectively) and are outlined in Table 2. No cumulus parameterization was used in WRF D2 and D3, since the consistency of using such a scheme is uncertain for grid distances of 1–10 km as convection is increasingly explicitly resolved [*Kain*, 2004]. The simulations used the adaptive time stepping scheme, in which the time step is adjusted during runtime depending on the stability of both vertical and horizontal motions [*Hutchinson*, 2009]. This scheme greatly decreased the completion time, since time steps up to 4 s could be used in the finest resolution domain compared with a stable fixed time step of only 1 s.

In the default USGS land use data, glaciers in the Langtang catchment are almost absent. Therefore, the glacier mask in all domains was updated using the Randolph Glacier Inventory v. 3.2 [*Pfeffer et al.*, 2014], using a 40% threshold to define a grid cell as glaciated (see *Collier et al.* [2013, 2015]. The CMB model computes the column specific mass balance from solid precipitation, surface and subsurface melt, refreezing and liquid water storage in the snowpack, and surface vapor fluxes. The model solves the surface energy balance to determine the energy available for surface melt and resolves the glacier subsurface down to a depth of 9.0 m. For glacier pixels, the CMB model updates surface and subsurface fields (e.g., temperature, roughness, albedo and snow depth, extent, and bulk density), while for nonglaciated grid cells, prognosis of the surface and subsurface fields and fluxes is performed by the Noah-multiparameterization (MP) land surface model [*Niu et al.*, 2011]. Further information about the interactive coupling between the CMB model and WRF are given in *Collier et al.* [2013]. For this study, we employ the coupled model because it shows improved performance in glacierized catchments [*Collier et al.*, 2013]; however, we focus our analysis on simulated meteorological variability and precipitation processes.

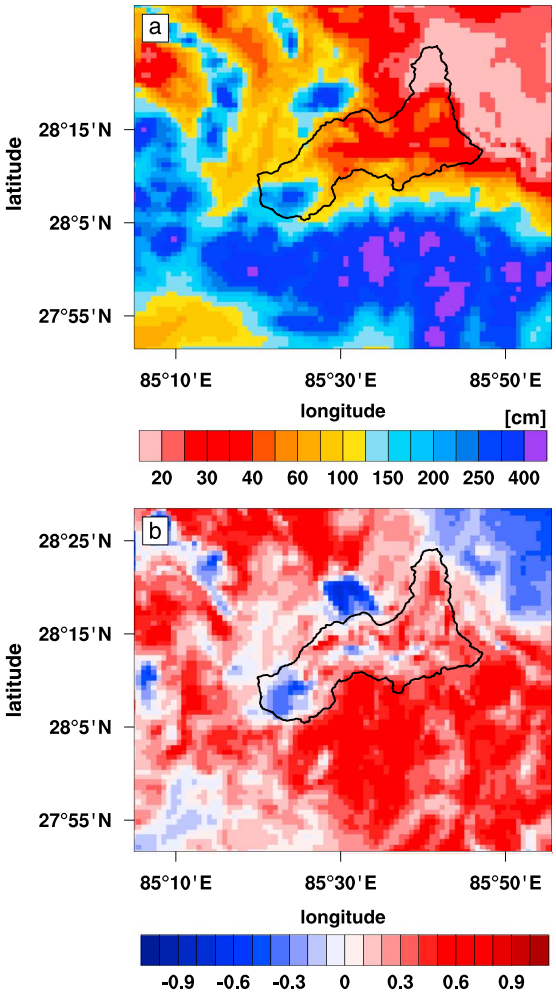

Figure 5. (a) Accumulated precipitation (cm) over the monsoon season in the Langtang catchment and surrounding area. (b) Cross correlation between daily total precipitation and daily mean lower level meridional winds, which were averaged over the lowest 10 model levels or 65 hPa.

The outer WRF domain (D1; 25 km grid spacing) was forced at its lateral boundaries by the full-resolution ERA-Interim reanalysis [*Dee et al.*, 2011], which has spatial and temporal resolutions of 0.75°×0.75° and 6 h, respectively. Grid analysis nudging was used on the horizontal winds, potential temperature, and water vapor mixing ratio fields in WRF D1 only. We employed this technique because it has been found to improve simulated means, variability, and extremes [*Otte et al.*, 2012] and reduce errors in the large-scale circulation [*Bowden et al.*, 2013] over longer reanalysis-driven simulations. However, nudging was only applied outside of the planetary boundary layer and above the lowest 15 model levels, and we used coefficients for winds, temperature, and humidity of 1.e-4, 1.e-4, and 5.e-5 s^{-1}, respectively, which are one third of both the default values in WRF and those used by *Otte et al.* [2012]. These modifications gave improved agreement with observed monsoon precipitation during the test simulations.

The initial snow condition obtained from ERA-Interim has unrealistic depths over the Karakoram (more than 20 m), as a result of the reanalysis' initialization procedure over large glaciers and interpolation by the WRF preprocessing programs [*Collier et al.*, 2013], which cause model instability. Therefore, we limited the initial snow depth in the Karakoram to 1 m and assumed an initial density of 300 kg m^3. We include 2 weeks of model spin-up, from 1 to 16 June 2012, over which period subsurface soil moisture fields stabilize prior to the onset of the monsoon, followed by the annual simulation from 17 June 2012 to 16 June 2013. The simulations were one-way, for clearer comparison of model performance in all three domains with the observational network. The run was performed on 192 processors of the Cartesius cluster of the SURFsara Supercomputing Center (www.surfsara.nl) and required approximately 15 days to complete.

2.3. Analysis Methods

For comparing the simulations with the observations, model data were taken from the closest grid point to each station without interpolation or height correction. Missing time periods in the observations were also discarded in the simulation data. Snow depth data from stations 10 and 11 (measured with a Campbell SR50A sonic ranging sensor) were averaged daily and corrected for 2% of the maximum distance measured between the sensor and the surface to remove noise in the data set.

For data analyses, we denote vertical averages of meteorological fields between 300 and 150 hPa and over the lowest 100 hPa as upper level and lower level, respectively. Spectral analyses of the valley winds are performed using the specx_anal function in National Center for Atmospheric Research Command Language (www.ncl.ucar.edu), after removing the series mean and using smoothing and tapering options of 5 and 0.10, respectively. The spectra were normalized by the maximum variance in the monsoon and winter seasons, considering a period of up to 5 days. Vertical lapse rates were computed as temporal and areal averages

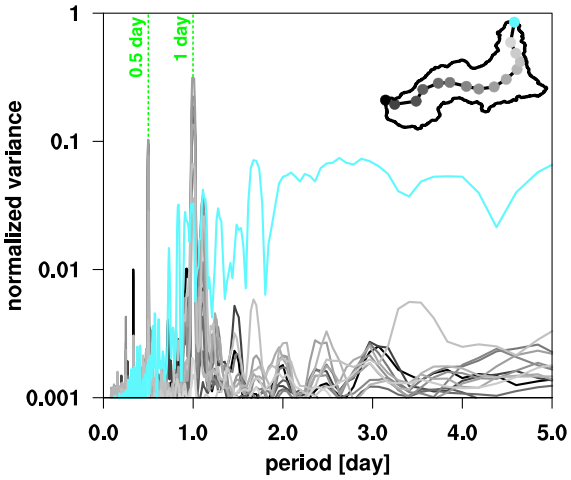

Figure 6. Normalized spectral density functions of wind speed, taken from the lowest model level at 15 points on the along-valley profile shown in the map in the upper right corner. Note the logarithmic *y* axis.

in 200 m elevation bins, while the cross- and along-valley profiles were computed using seasonal mean or total fields along the transects shown in Figure 1a. The daily air temperature lapse rates were computed using linear regression of hourly data [*Petersen and Pellicciotti*, 2011] over the catchment, from which daily minima, means, and maxima were computed.

3. Results

In section 3.1, we first evaluate simulated meteorological fields in the Langtang catchment in all three model domains using the observational data set outlined in section 2.1. In section 3.2, we present a brief overview of annual conditions in the finest resolution domain, D3. Finally, in sections 3.3 and 3.4, we discuss meteorological variability in the catchment during the monsoon and winter seasons, respectively, as represented in D3.

3.1. Model Evaluation

In Figure 2, we compare modeled and observed (i) terrain height and (ii) daily mean near-surface air temperature over the year for all three domains. D3 provides the most realistic representation of the terrain, while D1 and D2 strongly overestimate topographic height, by 1.5 and 1.1 km on average because many of observational sites are located in the valley (Figure 2a). As a result, there is a strong bias in near-surface air temperature ($T_{2\,m}$), which is highest in the two coarsest-resolution domains (Figure 2b). Increasing the grid spacing to 1 km greatly improves both the root-mean-square deviation (RMSD) in $T_{2\,m}$ and the simulated daily variability (cf. numbers provided above Figure 2b).

The model captures the strong seasonal variability in the frequency and magnitude of precipitation events over the year, as well as the rapid transition between the monsoon and the postmonsoon seasons (Figure 3a). During the monsoon season, however, the simulations underestimate precipitation at all sites where data are available (Figures 3a and 3b). In particular, the model has difficulties in capturing the strong increase in accumulated precipitation between stations one and two at any resolution, since this area coincides with a strong rise in elevation over a short horizontal distance (mean and 95th percentile gradients of 11 and 35%) in a narrow and curved part of the valley. Aside from this feature, the along-valley variability in accumulated precipitation is best represented in D3, since the catchment is represented by only three grid points in D1, and D2 simulates a decrease in precipitation both upvalley and upslope (e.g., between sites 5 and 6 and site 10). At the highest-altitude station (10), D3 captures part of the observed upslope increase in precipitation and provides the best correlation with observed daily totals ($R^2 = 0.02$, 0.09, and 0.24 in D1–D3, respectively). Simulated precipitation in D3 also has the lowest annual RMSD (cf. numbers in Figure 3a) and mean deviation over the monsoon period (MD; observed minus modeled; MD = 32, 43, and 29 cm in D1–D3, respectively).

The mean observed diurnal cycle of precipitation confirms the importance of both daytime convective and nighttime stratiform components during the monsoon season (Figure 3c) [e.g., *Ueno and Yamada*, 1990; *Ueno et al.*, 1993]. While all domains underestimate the amount of precipitation during the night and early morning, D3 provides better agreement in the magnitudes of convective precipitation in the afternoon and early evening (Figure 3c). We note that the aforementioned underestimate of forested areas in the Langtang could contribute to the discrepancy in nocturnal precipitation, through either overestimation of surface radiative cooling or erroneous representation of moisture-convection feedbacks, which can significantly impact diurnal cycles of precipitation in cloud-resolving simulations in alpine terrain [*Hohenegger et al.*, 2009].

The poorer performance of D2 during the monsoon season compared with D1 despite the increased spatial resolution may in part result from neglecting a cumulus parameterization, as the explicit simulation of

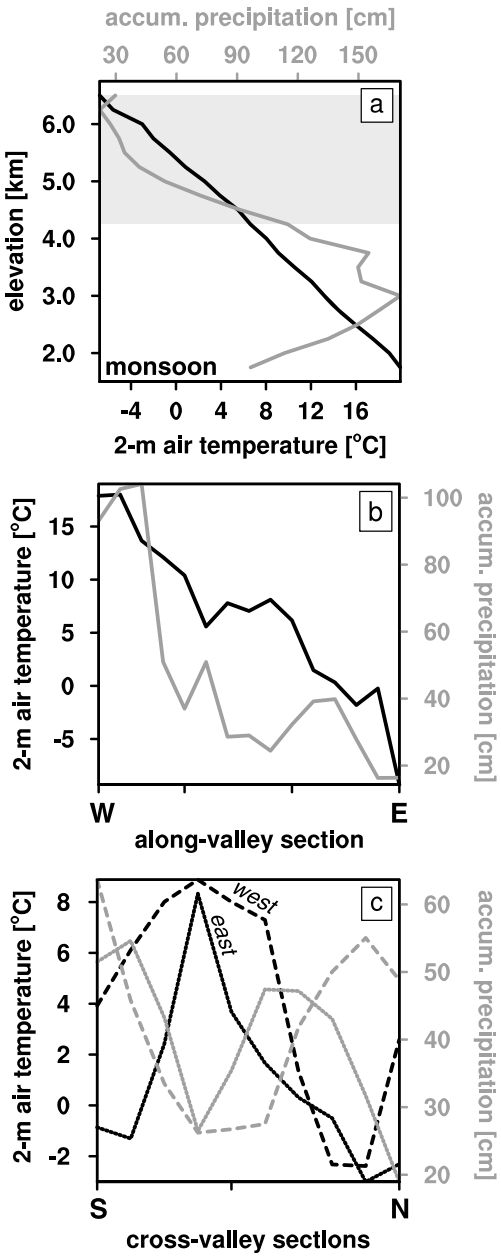

Figure 7. Gradients of simulated mean 2 m air temperature (black curve; [°C]) and accumulated all-phase precipitation (grey curve, [cm]) during the monsoon season, computed (a) as a function of elevation in 250 m height bins (glaciated elevations are shaded in light grey) and on the (b) along-valley and (c) cross-valley sections whose locations are delineated in Figure 1a. The *x* axis labels of Figures 7b and 7c correspond to the section start and end points (in Figure 1a). Note that the scale for accumulated precipitation starts above 0 cm in all panels. For Figure 7c, the short and long dashed curves show data from the east and west cross sections, respectively.

nonhydrostatic motions in deep convection may be inadequate at 5 km grid spacing [*Weisman et al.*, 1997]. However, a brief test simulation of the monsoon season indicates that the inclusion of a cumulus parameterization in D2 worsens the agreement with observations in the Langtang catchment (the mean deviation increases to 48 cm and precipitation decreases strongly between stations one and two), in contrast to the findings of *Langhans et al.* [2013]. This feature appears to be related to an overestimate of convective precipitation and thus moisture removal on the slopes to the south of the Langtang when a cumulus parameterization is included (not shown).

Precipitation during winter is accumulated during four events associated with the passage of midlatitude cyclones (Figure 3a; see section 3.4; approximate periods are 16–20 January, 3–9 February, 14–18 February, and 21–25 February). In contrast to the monsoon season, precipitation is mainly overestimated, in particular for the two events on 18 January and 15 February (Figure 3a). However, a contributing factor to the disagreement is likely the undercatch of snowfall in windy conditions [e.g., *Goodison et al.*, 1997]. Based on the correction of Gobulev [*Goodison et al.*, 1997, equation (1), p. 132], we estimate a mean snow undercatch of 20% during the four events, which is consistent with a slightly closer agreement between modeled and observed snow depths (Figure 3d). The timing of winter precipitation is well captured, as is the evolution of snow depth ($R^2 = 0.78$, 0.86, and 0.85 in D1–D3). The smaller differences in modeled precipitation between model domains but higher magnitudes of snow accumulation for D2 and D3 are consistent with previous studies in complex terrain in winter [*Rasmussen et al.*, 2011; *Prein et al.*, 2013b]. Accumulation at site 10 is representative of the variability and magnitude of the catchment mean (dashed line in Figure 3d), since the forcing in this season is synoptic-scale and the elevation of the site is close to the modeled catchment mean (4831 versus 4930 m asl, respectively).

3.2. Annual Contrasts in Meteorological Conditions

Figure 4 shows the strong contrast in simulated atmospheric conditions in D3 over the year. The monsoon period is characterized by minimal upper level westerly circulation (e.g., low or slight negative upper level zonal winds), the warmest and most humid conditions, and the highest mixing ratios of microphysical tracers. These conditions are consistent with the daily intense precipitation events (cf. Figure 3a). The postmonsoon period is characterized by an increasing influence of the westerlies, strong cooling and drying of the atmosphere, and a near absence of hydrometeors. As a result, precipitation is rare during this period. During the winter season, a small number (~4) of synoptic disturbances passed over the Himalaya, which are associated with positive spikes in meridional velocity, air

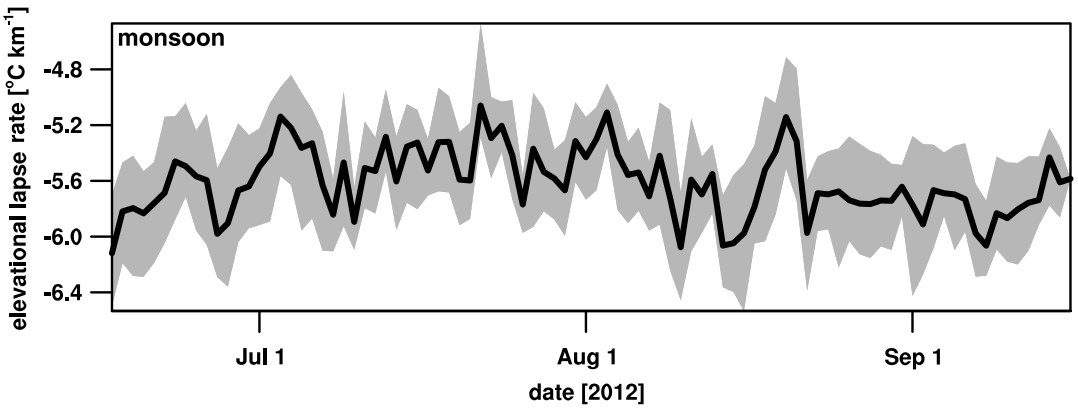

Figure 8. A time series of the simulated elevational lapse rate in 2 m air temperature (°C km^{-1}) over the monsoon period. The black curve indicates the daily mean value, while the grey band shows the daily range.

temperature, and microphysical tracers. Finally, the premonsoon period shows a transition back toward monsoon-dominated conditions and an associated increase in the frequency of precipitation events. Further analysis of meteorological conditions in the Langtang catchment will focus on the two seasons with the most contrasting conditions, the monsoon and winter periods.

3.3. Monsoon Season

Precipitation during the monsoon season mainly accumulates on the slopes to the south of the Langtang catchment and at the valley entrance, with a clear drying trend upvalley (Figure 5a). Variations in daily precipitation show strong positive correlations with precipitable water over the region indicated in Figure 5a (not shown). In addition, this region is strongly influenced by monsoon activity, with positive correlations between daily total precipitation and daily mean lower level meridional winds along the slopes of the valley and south of the catchment (Figure 5b). Precipitation is primarily accrued during active phases of the monsoon (spatially averaged value of 93 cm compared to 150 cm in total over the monsoon season, with active days computed following *Prasad and Hayashi* [2007] using ERA-Interim data between 2004 and 2014).

Spectral analysis of the valley wind speeds indicates that, along most of the valley profile, the circulation during the monsoon season is dominated by flows with diurnal and half-day periods (Figure 6), a feature that is not exhibited by the winds aloft. Thus, in these regions of the catchment, thermally driven regional and local valley circulations act as the drivers of precipitation. The precipitation maximum near the entrance is likely produced by channeling of such flows over the aforementioned steep topography between sites 1 and 2, as supported by a strong negative (positive) correlation with relative humidity (upslope winds) in this area. The improvements in simulated precipitation in D3 compared with D1 and D2 (cf. section 3.1) are likely related to better representation of the along-valley winds contributing to convective precipitation where atmospheric stability conditions are favorable [*Langhans et al.*, 2013]. On the other hand, the point located furthest upvalley has more variance at superdiurnal and synoptic-scale periods, from which we infer that this site is primarily exposed to the large-scale flow.

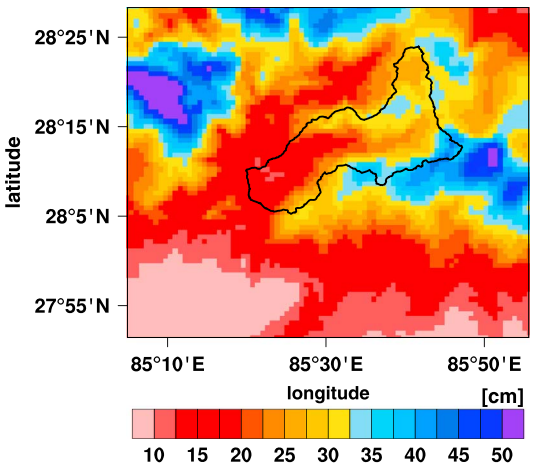

Figure 9. Accumulated precipitation (cm) over the winter period in the Langtang catchment.

Mean-modeled 2 m air temperature in the Langtang ranges linearly from ~20 to −7°C between 1750 and 6500 m (Figure 7a). Accumulated precipitation during the monsoon, averaged over the entire

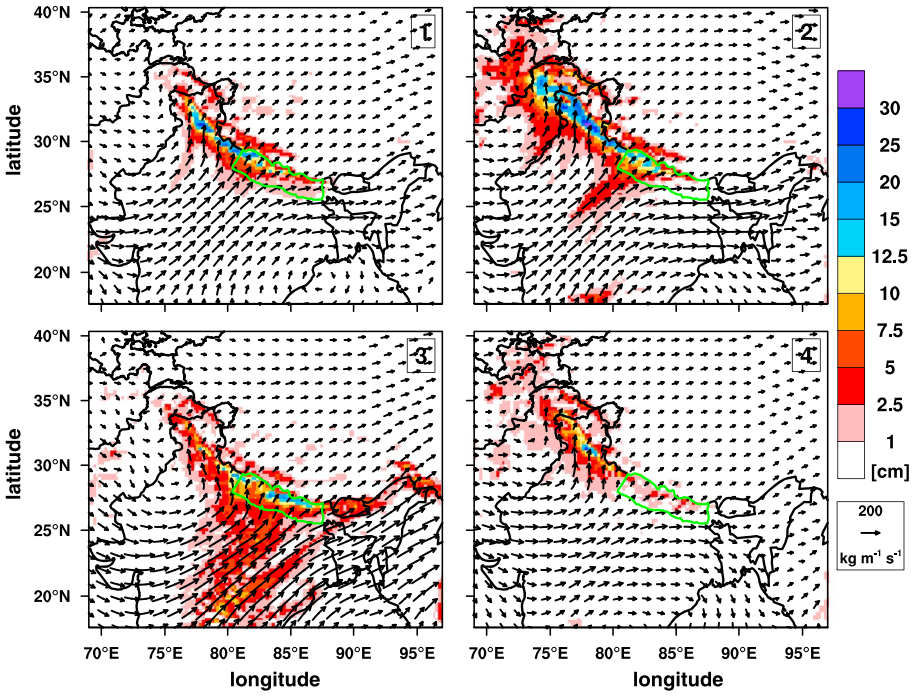

Figure 10. Total precipitation shaded in (cm) and vertically integrated average moisture fluxes in (kg m^{-1} s^{-1}), for each of the four winter precipitation events associated with midlatitude cyclones. The approximate dates of events 1–4 are 16–20 January, 3–9 February, 14–18 February, and 21–25 February, respectively. The location of Nepal is shown by the green contour.

catchment, peaks at an elevation around 3000 m and decreases almost linearly at higher and lower altitudes. The along-valley variation of monsoon precipitation ranges from around 100 cm near the entrance of the valley to less than 10 cm in the most upstream part (Figure 7b). Below ~4500 m, frozen fraction is ~0%, and above this level, the frozen fraction increases linearly up to 50% (not shown). The cross-valley profiles of precipitation show that the valley floor is the driest and precipitation increases significantly upslope by approximately a factor of 2 (Figure 7c). Mean near-surface air temperature is strongly related to topographic height ($R^2 = 0.96$), which gives a cooling trend upvalley and between the valley floor and surrounding ridges (Figures 7b and 7c).

Temporal variability in daily mean air temperature corresponds with that of net radiation along the valley floor and at both the entrance and north ridges and with that of downwelling longwave radiation along the slopes and in the upper valley (not shown). During the monsoon season, the lapse rate (LR) of near-surface air temperature varies from −6.5 to −4.5°C km^{-1}, with an average value of −5.6°C km^{-1} (Figure 8). The mean-simulated LR at the observational sites (−5.1°C km^{-1}) is slightly steeper than the measured value (−4.6°C km^{-1}). However, the difference may be attributed in part to an overestimation of the high-altitude temperature observations due to the use of unaspirated temperature sensors [*Immerzeel et al.*, 2014].

3.4. Winter Season

Total precipitation in winter is highest along the southern ridge of the catchment and, in contrast to the monsoon season, at higher elevations, while the valley entrance and floor are much drier (Figure 9). Precipitation accumulates during four distinct and relatively large events associated with the passage of midlatitude low-pressure systems (cf. four peaks in Figure 2a and section 3.1). The cyclonic circulation associated with these systems produces (i) positive thermal and moisture advection northward, with the latter originating primarily in the Arabian Sea (Figure 10), and (ii) lower level winds that are more perpendicular to the orographic arc. Higher precipitation intensities over Nepal, in particular during the first three events, are associated with greater moisture advection into the region (Figure 10) and stronger cross-barrier winds

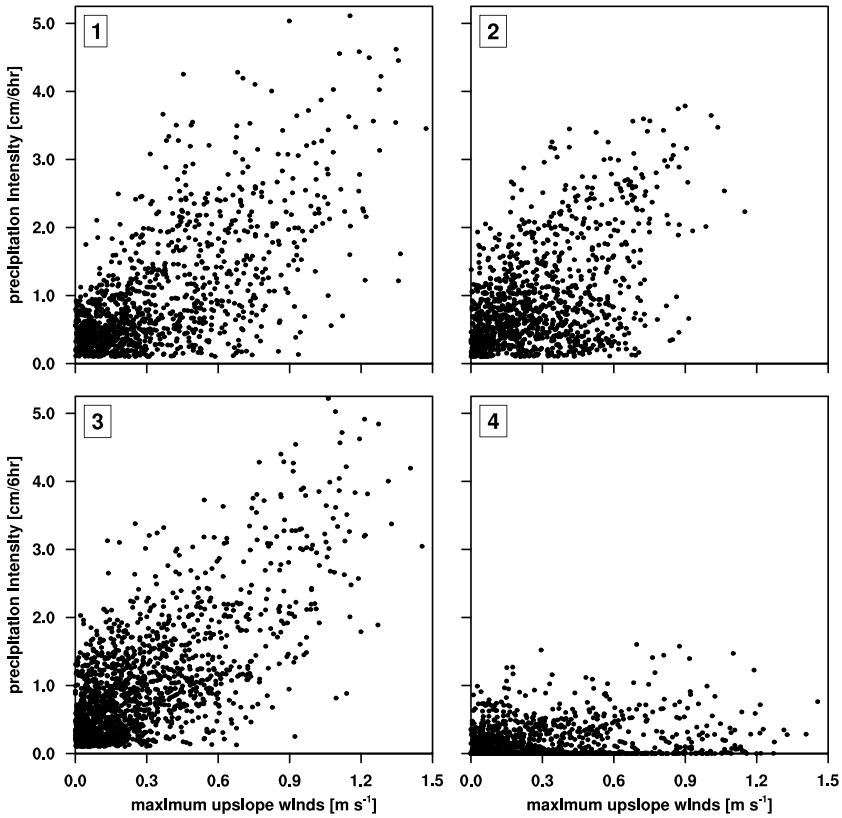

Figure 11. Scatterplots of precipitation intensities (cm 6 h^{-1}) versus maximum lower level upslope winds in (m s^{-1}) considering the lowest 12 model levels (~100 hPa above the surface) in Nepal for each of the four winter events.

(Figure 11). Events 1–3 are driven by a relatively deeper trough west of the Himalayas, with the 5700 m geopotential height contour at the 500 hPa level extending below 23°N, compared with ~25°N in the fourth event and its mean latitudinal position of ~30°N in winter (not shown). The precipitation magnitudes and processes are consistent with the findings of WRF simulations of two dynamically driven winter cyclone events [*Norris et al.*, 2015] and with hypothesized drivers of accumulation in this season [*Lang and Barros*, 2004]. Consistent with these processes, the power spectra of valley wind speeds in winter do not show a single, pronounced diurnal peak and have higher spectral densities at longer periods (Figure 12). Thus, as expected, superdiurnal and synoptic-scale motions are the dominant part of the valley circulation, and the contribution to the wind speed variance by such flows increases upvalley.

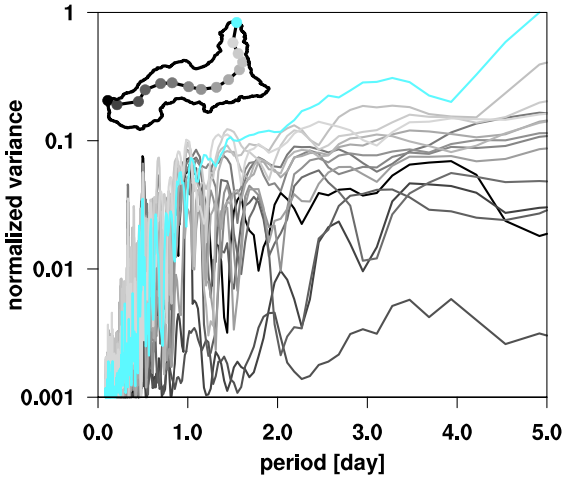

Figure 12. Same as Figure 6 but for the winter season.

Averaged over the Langtang catchment, simulated mean 2 m air temperature ranges linearly from ~9 to −24°C between 1750 and 6500 m (Figure 13a). Total precipitation is greatest at higher (and glaciated) elevations, increasing from ~15 to 30 cm between 3000 and 6500 m, which is in contrast to the monsoon season and confirms the seasonal differences indicated by *Seko* [1987] on the basis of four observational stations. In these simulations, the elevation range of peak precipitation extends approximately 1 km higher

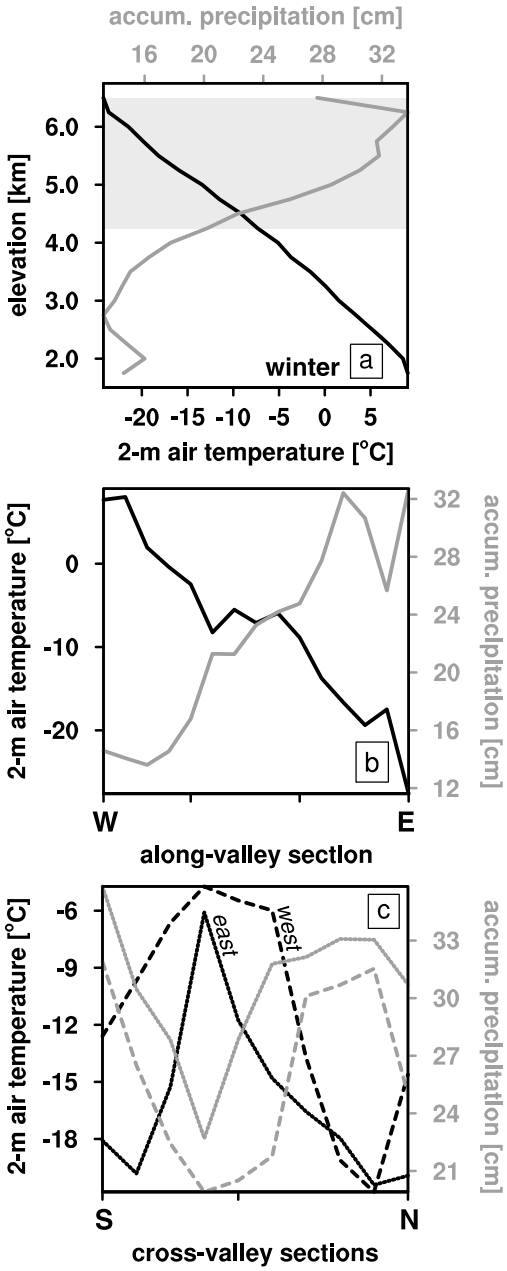

Figure 13. Same as Figure 7 but for the winter season.

than the range reported by *Norris et al.* [2015]; however, the difference is congruent with the lower grid spacing in their study (6.7 km). The frozen fraction increases linearly from ~10% below 2000 m to 90% above 3500 m (not shown). Along valley, there is a large variation in precipitation ranging from around 14 cm near the entrance to 32 cm in the upper parts of the valley. Congruent with the elevational distributions, air temperature decreases while accumulated precipitation increases both along the valley transect and between the valley floor and surrounding ridges (Figures 13b and 13c). The LR of air temperature varies from −10.0 to −5.1°C km^{-1} over the winter season, with an average value of −7.9°C km^{-1} (Figure 14). During precipitation events, the LR is less negative (highlighted in blue), due to positive thermal advection by the cyclonic circulation. However, immediately following such events, it becomes more negative, as a result of differential snow accumulation with altitude (cf. Figure 13a). At the observational sites, the model again overestimates the LR (−6.7°C km^{-1} compared with −5.8° C km^{-1} measured), with the stronger bias in winter likely related to the overestimation of snowfall that is concentrated at higher elevations (cf. Figures 3d and 3a).

4. Discussion and Conclusions

In this study, the WRF-CMB model, configured with three nested domains of 25, 5, and 1 km grid spacing, was used to perform a 1 year simulation of atmospheric dynamics in the high-altitude Langtang catchment in the Nepalese Himalaya. The simulations were evaluated using a unique high-altitude observational data set, which showed that local meteorological variability in the catchment was best captured in the 1 km domain, with the finer representation of orography and explicit simulation of convection in this domain yielding strong improvements in near-surface air temperature and smaller improvements in precipitation (in particular at the highest-altitude station).

Subsequent analysis focused on high-resolution patterns of near-surface meteorological fields and precipitation processes between the contrasting monsoon and winter seasons, which revealed

1. a reversal in the vertical gradient of precipitation, with peak values at ~3000 m located near the valley entrance during the monsoon compared with ~5000–6000 m located along the ridges in winter, and
2. a stronger lapse rate of near-surface air temperature and greater diurnal variability associated with synoptic disturbances in winter compared with the monsoon season.

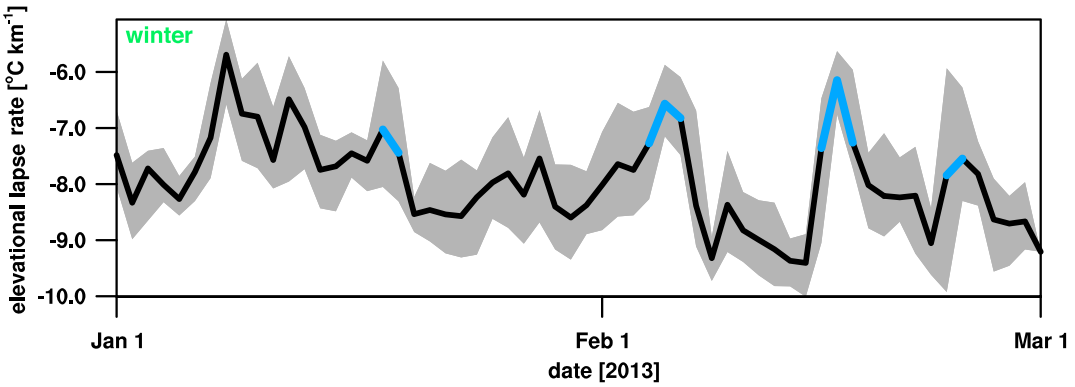

Figure 14. Same as Figure 8 but for the winter season. The blue lines highlight the days where daily total area-averaged precipitation in the catchment exceeds 0.1 cm.

The simulations also confirmed the dominance of thermally driven regional and local valley winds that produce near-daily precipitation during the monsoon season, compared with a largely synoptic-scale influence in winter and accumulation magnitudes linked to moisture advection and cross-barrier winds during the passage of midlatitude low-pressure systems. The simulated patterns are congruent with previous observational studies in the Langtang catchment [e.g., *Seko*, 1987] and of high relevance for the ongoing glacio-hydrological research in the Langtang catchment and Himalayas in general.

The improved representation of meteorological variability in alpine terrain, in particular during summer, in cloud-resolving simulations (Δx~O(1 km)) compared with coarser ones, is consistent with numerous previous studies [e.g., *Rasmussen et al.*, 2011; *Horvath et al.*, 2012; *Langhans et al.*, 2013; *Prein et al.*, 2013a, 2013b]. However, even in the 1 km domain, significant biases in precipitation were found during the monsoon season and the key feature of the strong increase in accumulation between stations 1 and 2 was not captured. Although *Langhans et al.* [2012] demonstrated convergent behavior in kilometer-scale real-case simulations of moist convection in complex terrain, other idealized studies have found that a grid spacing much smaller than 1 km is needed to adequately resolve the characteristic length scale and evolution of the moist convective elements studied (*Bryan et al.* [2003] and *Craig and Dörnbrack* [2008] suggest as low as 10–100 m). In addition, we suggest that the representation of the terrain at 1 km may be insufficient in this case to resolve certain topographic features, such as the peak gradient (35%) between sites 1 and 2 and the narrowest parts of the valley (<~2 km). Thus, future work should assess the potential of subkilometer resolution simulations in the Langtang for improving the overall monsoon precipitation statistics, as well as the representation of terrain-associated processes, such as the local enhancement of precipitation by steep windward ridges [*Medina and Houze*, 2003; *Garvert et al.*, 2007] and daytime mountain valley wind system [*Schmidli and Rotunno*, 2010; *Schmidli et al.*, 2011]. Finally, the impact of errors in the surface fields mentioned in section 2.1 should be investigated through the incorporation of higher-resolution topographic and land use data sets.

In our simulations, we identify a strong underestimation of orographic precipitation over the central Himalayas in D1, with a particularly erroneous representation of variability in local meteorological conditions in the Langtang. The grid spacing of this domain (25 km) is comparable to the resolution of gridded observed data products available for the Himalaya (e.g., Tropical Rainfall Measuring Mission [*Huffman et al.*, 2007] and Asian Precipitation–Highly Resolved Observational Data Integration Towards Evaluation [*Yatagai et al.*, 2012]) and much finer than general circulation models and commonly used atmospheric reanalyses [*Uppala et al.*, 2005]. Nonetheless, all of these data sources have, in the absence of higher-resolution products, been used to analyze high-altitude meteorological conditions in High Asia without statistical corrections for orographic effects [e.g., *Bookhagen and Burbank*, 2010; *Kapnick et al.*, 2014; *Lutz et al.*, 2014]. We therefore conclude that using high-resolution atmospheric models to generate meteorological forcing data, in combination with high-altitude observational data for evaluation, provides great potential for improving the quality and local accuracy of climate change impact studies in the Himalaya.

Acknowledgments
The simulation data can be obtained through the corresponding author. The authors thank the following project partners for their help in facilitating this study, for providing data, and for assisting in the fieldwork: ETH, ICIMOD, the Himalayan Cryosphere, Climate and Disaster Research Center of Kathmandu University, and the Department of Hydrology and Meteorology and the Department of National Parks and Wildlife Conservation of the Government of Nepal. This study was partially funded by the Netherlands Organization for Scientific Research (NWO) through their VENI program, by the South Asia Research Hub of the UK Department for International Development and by the Himalayan Adaptation, Water and Resilience (HI-AWARE) project under the Collaborative Adaptation Research Initiative in Africa and Asia (CARIAA), with financial support from the UK Government's Department for International Development, and the International Development Research Centre in Ottawa, Canada. Supercomputing resources were financially supported by NWO and provided by SURFsara (www.surfsara.nl) on the Cartesius cluster and by WestGrid (www.westgrid.ca) and Compute Calcul Canada (www.computecanada.ca) on the Bugaboo cluster.

References

Barros, A. P., G. Kim, E. Williams, and S. W. Nesbitt (2004), Probing orographic controls in the Himalayas during the monsoon using satellite imagery, *Nat. Hazards Earth Syst. Sci.*, *4*(1), 29–51, doi:10.5194/nhess-4-29-2004.

Bookhagen, B., and D. W. Burbank (2006), Topography, relief, and TRMM-derived rainfall variations along the Himalaya, *Geophys. Res. Lett.*, *33*, L08405, doi:10.1029/2006GL026037.

Bookhagen, B., and D. W. Burbank (2010), Toward a complete Himalayan hydrological budget: Spatiotemporal distribution of snowmelt and rainfall and their impact on river discharge, *J. Geophys. Res.*, *115*, F03019, doi:10.1029/2009JF001426.

Bowden, J. H., C. G. Nolte, and T. L. Otte (2013), Simulating the impact of the large-scale circulation on the 2-m temperature and precipitation climatology, *Clim. Dyn.*, *40*, 1903–1920, doi:10.1007/s00382-012-1440-y.

Bryan, G. H., J. C. Wyngaard, and J. M. Fritsch (2003), Resolution requirements for the simulation of deep moist convection, *Mon. Weather Rev.*, *131*(10), 2394–2416.

Collier, E., T. Mölg, F. Maussion, D. Scherer, C. Mayer, A. B. G. B. G. Bush, and W. W. Immerzeel (2013), High-resolution interactive modelling of the mountain glacier–atmosphere interface: An application over the Karakoram, *Cryosphere*, *7*, 779–795, doi:10.5194/tc-7-779-2013.

Collier, E., F. Maussion, L. I. Nicholson, T. Mölg, W. W. Immerzeel, and A. B. G. Bush (2015), Impact of debris cover on glacier ablation and atmosphere-glacier feedbacks in the Karakoram, *Cryosphere*, *9*, 1617–1632, doi:10.5194/tc-9-1617-2015.

Collins, W. D., et al. (2004), Description of the NCAR Community Atmosphere Model (CAM 3.0), *Ncar/Tn-464+Str*, 214.

Craig, G. C., and A. Dörnbrack (2008), Entrainment in cumulus clouds: What resolution is cloud-resolving?, *J. Atmos. Sci.*, *65*(12), 3978–3988.

Dee, D. P., et al. (2011), The ERA-Interim reanalysis: Configuration and performance of the data assimilation system, *Q. J. R. Meteorol. Soc.*, *137*(656), 553–597, doi:10.1002/qj.828.

Fujita, K., A. Sakai, T. T. B. Chhetri, and K. S. A. C. T. B. Fujita (1997), Meteorological observation in Langtang Valley, Nepal Himalayas, 1996, *Bull. Glacier Res.*, *15*, 71–78.

Garvert, M. F., B. Smull, and C. Mass (2007), Multiscale mountain waves influencing a major orographic precipitation event, *J. Atmos. Sci.*, *64*(3), 711–737.

Goodison, B. E., P. Y. T. Louie, and D. Yang (1997), The WMO solid precipitation measurement intercomparison.

Hohenegger, C., P. Brockhaus, C. S. Bretherton, and C. Schär (2009), The soil moisture-precipitation feedback in simulations with explicit and parameterized convection, *J. Clim.*, *22*(19), 5003–5020, doi:10.1175/2009JCLI2604.1.

Horvath, K., D. Koracin, R. Vellore, and J. Jiang (2012), Sub-kilometer dynamical downscaling of near-surface winds in complex terrain using WRF and MM5 mesoscale models, *J. Geophys. Res.*, *117*, D11111, doi:10.1029/2012JD017432.

Huffman, G. J., R. F. Adler, D. T. Bolvin, G. Gu, E. J. Nelkin, K. P. Bowman, Y. Hong, E. F. Stocker, and D. B. Wolff (2007), The TRMM Multisatellite Precipitation Analysis (TMPA): Quasi-global, multiyear, combined-sensor precipitation estimates at fine scales, *J. Hydrometeorol.*, *8*(1), 38, doi:10.1175/JHM560.1.

Hutchinson, T. A. (2009), An adaptive time-step for increased model efficiency, in *23rd Conference on Weather Analysis and Forecasting/19th Conference on Numerical Weather Prediction*.

Immerzeel, W. W., F. Pellicciotti, and M. F. P. Bierkens (2013), Rising river flows throughout the twenty-first century in two Himalayan glacierized watersheds, *Nat. Geosci.*, *6*(9), 742–745.

Immerzeel, W. W., L. Petersen, S. Ragettli, and F. Pellicciotti (2014), The importance of observed gradients of air temperature and precipitation for modeling runoff from a glacierised watershed in the Nepalese Himalayas, *Water Resour. Res.*, *50*, 2212–2226, doi:10.1002/2013WR014506.

Jiménez, P. A., J. Dudhia, J. F. González-Rouco, J. Navarro, J. P. Montávez, and E. García-Bustamante (2012), A revised scheme for the WRF surface layer formulation, *Mon. Weather Rev.*, *140*(3), 898–918.

Kain, J. S. (2004), The Kain–Fritsch convective parameterization: An update, *J. Appl. Meteorol.*, *43*, 170–181, doi:10.1175/1520-0450(2004)043<0170:TKCPAU>2.0.CO;2.

Kapnick, S. B., T. L. Delworth, M. Ashfaq, S. Malyshev, and P. C. D. Milly (2014), Snowfall less sensitive to warming in Karakoram than in Himalayas due to a unique seasonal cycle, *Nat. Geosci.*, *7*, 834–840, doi:10.1038/ngeo2269.

Kumar, P., S. Kotlarski, C. Moseley, K. Sieck, H. Frey, M. Stoffel, and D. Jacob (2015), Response of Karakoram-Himalayan glaciers to climate variability and climatic change: A regional climate model assessment, *Geophys. Res. Lett.*, *42*, 1818–1825, doi:10.1002/2015GL063392.

Lang, T. J., and A. P. Barros (2004), Winter storms in the central Himalayas, *J. Meteorol. Soc. Japan*, *82*(3), 829–844, doi:10.2151/jmsj.2004.829.

Langhans, W., J. Schmidli, and C. Schär (2012), Bulk convergence of cloud-resolving simulations of moist convection over complex terrain, *J. Atmos. Sci.*, *69*(7), 2207–2228.

Langhans, W., J. Schmidli, O. Fuhrer, S. Bieri, and C. Schar (2013), Long-term simulations of thermally driven flows and orographic convection at convection-parameterizing and cloud-resolving resolutions, *J. Appl. Meteorol. Climatol.*, *52*(6), 1490–1510, doi:10.1175/JAMC-D-12-0167.1.

Leroy, M., et al. (2007), GlobCover: A 300 m global land cover product for 2005 using Envisat MERIS time series, in *Proceedings of the ISPRS Commission VII Mid-Term Symposium*, pp. 8–11.

Lundquist, J. D., N. Pepin, and C. Rochford (2008), Automated algorithm for mapping regions of cold-air pooling in complex terrain, *J. Geophys. Res.*, *113*, D22107, doi:10.1029/2008JD009879.

Lutz, A. F., W. W. Immerzeel, A. B. Shrestha, and M. F. P. Bierkens (2014), Consistent increase in High Asia's runoff due to increasing glacier melt and precipitation, *Nat. Clim. Chang.*, *4*(7), 587–592, doi:10.1038/nclimate2237.

Maussion, F., D. Scherer, T. Mölg, E. Collier, J. Curio, and R. Finkelnburg (2014), precipitation seasonality and variability over the Tibetan Plateau as resolved by the High Asia Reanalysis*, *J. Clim.*, *27*(5), 1910–1927.

Medina, S., and R. A. Houze Jr. (2003), Air motions and precipitation growth in Alpine storms, *Q. J. R. Meteorol. Soc.*, *129*(588), 345–371.

Minder, J. R., P. W. Mote, and J. D. Lundquist (2010), Surface temperature lapse rates over complex terrain: Lessons from the Cascade Mountains, *J. Geophys. Res.*, *115*, D14122, doi:10.1029/2009JD013493.

Mölg, T., N. J. Cullen, D. R. Hardy, G. Kaser, and L. Klok (2008), Mass balance of a slope glacier on Kilimanjaro and its sensitivity to climate, *Int. J. Climatol.*, *28*(7), 881–892.

Mölg, T., J. C. H. Chiang, A. Gohm, and N. J. Cullen (2009), Temporal precipitation variability versus altitude on a tropical high mountain: Observations and mesoscale atmospheric modelling, *Q. J. R. Meteorol. Soc.*, *135*(643), 1439–1455.

Mölg, T., F. Maussion, and D. Scherer (2014), Mid-latitude westerlies as a driver of glacier variability in monsoonal High Asia, *Nat. Clim. Chang.*, *4*(1), 68–73, doi:10.1038/nclimate2055.

Morinaga, Y., K. Seko, and S. Takahashi (1987), Seasonal variation of snowline in Langtang Valley, Nepal Himalayas, 1985–1986, *Bull. Glacier Res.*, *5*, 49–53.

Morrison, H., G. Thompson, and V. Tatarskii (2009), Impact of cloud microphysics on the development of trailing stratiform precipitation in a simulated squall line: Comparison of one- and two-moment schemes, *Mon. Weather Rev.*, *137*, 991–1007, doi:10.1175/2008MWR2556.1.

Nakanishi, M., and H. Niino (2006), An improved Mellor–Yamada level-3 model: Its numerical stability and application to a regional prediction of advection fog, *Boundary Layer Meteorol.*, *119*(2), 397–407.

Niu, G.-Y., et al. (2011), The community Noah land surface model with multiparameterization options (Noah-MP): 1. Model description and evaluation with local-scale measurements, *J. Geophys. Res.*, *116*, D12109, doi:10.1029/2010JD015139.

Norris, F., L. M. Carvalho, C. Jones, and F. Cannon (2015), WRF simulations of two extreme snowfall events associated with contrasting extratropical cyclones over the western and central Himalaya, *J. Geophys. Res. Atmos.*, *120*, 3114–3138, doi:10.1002/2014JD022592.

Otte, T. L., C. G. Nolte, M. J. Otte, and J. H. Bowden (2012), Does nudging squelch the extremes in regional climate modeling?, *J. Clim.*, *25*(20), 7046–7066.

Palazzi, E., J. Von Hardenberg, and A. Provenzale (2013), Precipitation in the Hindu-Kush Karakoram Himalaya: Observations and future scenarios, *J. Geophys. Res. Atmos.*, *118*, 85–100, doi:10.1029/2012JD018697.

Petersen, L., and F. Pellicciotti (2011), Spatial and temporal variability of air temperature on a melting glacier: Atmospheric controls, extrapolation methods and their effect on melt modeling, Juncal Norte Glacier, Chile, *J. Geophys. Res.*, *116*, D23109, doi:10.1029/2011JD015842.

Pfeffer, W. T., et al. (2014), The Randolph Glacier Inventory: A globally complete inventory of glaciers, *J. Glaciol.*, *60*(221), 537–552.

Prasad, V. S., and T. Hayashi (2007), Active, weak and break spells in the Indian summer monsoon, *Meteorol. Atmos. Phys.*, *95*(1–2), 53–61.

Prein, A. F., A. Gobiet, M. Suklitsch, H. Truhetz, N. K. Awan, K. Keuler, and G. Georgievski (2013a), Added value of convection permitting seasonal simulations, *Clim. Dyn.*, *41*(9–10), 2655–2677, doi:10.1007/s00382-013-1744-6.

Prein, A. F., G. J. Holland, R. M. Rasmussen, J. Done, K. Ikeda, M. P. Clark, and C. H. Liu (2013b), Importance of regional climate model grid spacing for the simulation of heavy precipitation in the Colorado headwaters, *J. Clim.*, *26*(13), 4848–4857, doi:10.1175/JCLI-D-12-00727.1.

Ragettli, S., F. Pellicciotti, W. W. Immerzeel, E. S. Miles, L. Petersen, M. Heynen, J. M. Shea, D. Stumm, S. Joshi, and A. B. Shrestha (2014), Unraveling the hydrology of a Himalayan watershed through integration of high resolution in-situ data and remote sensing with an advanced simulation model, *Adv. Water Resour.*, *78*, 94–111.

Rasmussen, R., et al. (2011), High-resolution coupled climate runoff simulations of seasonal snowfall over Colorado: A process study of current and warmer climate, *J. Clim.*, *24*(12), 3015–3048, doi:10.1175/2010JCLI3985.1.

Scherler, D., B. Bookhagen, and M. R. Strecker (2011), Spatially variable response of Himalayan glaciers to climate change affected by debris cover, *Nat. Geosci.*, *4*(1), 156–159, doi:10.1038/ngeo1068.

Schmidli, J., and R. Rotunno (2010), Mechanisms of along-valley winds and heat exchange over mountainous terrain, *J. Atmos. Sci.*, *67*(9), 3033–3047, doi:10.1175/2010JAS3473.1.

Schmidli, J., et al. (2011), Intercomparison of mesoscale model simulations of the daytime valley wind system, *Mon. Weather Rev.*, *139*(5), 1389–1409, doi:10.1175/2010MWR3523.1.

Seko, K. (1987), Seasonal variation of altitudinal dependence of precipitation in Langtang Valley, Napal Himalayas, *Bull. Glacier Res.*, *5*, 41–47.

Seko, K., and S. Takahashi (1991), Characteristics of winter precipitation and its effect on glaciers in the Nepal Himalaya, *Bull. Glacier Res.*, 9–16.

Skamarock, W. C., and J. B. Klemp (2008), A time-split nonhydrostatic atmospheric model for Weather Research And Forecasting applications, *J. Comput. Phys.*, *227*(7), 3465–3485, doi:10.1016/j.jcp.2007.01.037.

Ueno, K., and T. Yamada (1990), Diurnal variation of precipitation in Langtang Valley, Nepal Himalayas, *Bull. Glacier Res.*, *8*, 93–101.

Ueno, K., T. Shiraiwa, and T. Yamada (1993), *Precipitation Environment in the Langtang Valley, Nepal Himalayas*, *IAHS Publ. 218*, pp. 207–219.

Uppala, S. M., et al. (2005), The ERA-40 re-analysis, *Q. J. R. Meteorol. Soc.*, *131*(612), 2961–3012, doi:10.1256/qj.04.176.

Weisman, M. L., W. C. Skamarock, and J. B. Klemp (1997), The resolution dependence of explicitly modeled convective systems, *Mon. Weather Rev.*, *125*(4), 527–548.

Yatagai, A., N. Yasutomi, A. Hamada, A. Kitoh, K. Kamiguchi, and O. Arakawa (2012), APHRODITE: Constructing a long-term daily gridded precipitation dataset for Asia based on a dense network of rain gauges, *Bull. Am. Meteorol. Soc.*, *93*(9), 1401–1415.